ACS Energy LETTERS

Cite This: ACS Energy Lett. 2019, 4, 352−357

http://pubs.acs.org/journal/aelccp

LETTER

$CaSnO_3$: An Electrocatalyst for Two-Electron Water Oxidation Reaction to Form H_2O_2

So Yeon Park,[†,‡,#] Hadi Abroshan,[§,#] Xinjian Shi,[‡,#] Hyun Suk Jung,[*,†] Samira Siahrostami,[*,§] and Xiaolin Zheng[*,‡]

[†]School of Advanced Materials Science & Engineering, Sungkyunkwan University, Suwon 16419, Republic of Korea

[‡]Department of Mechanical Engineering, Stanford University, 440 Escondido Mall, Stanford, California 94305, United States

[§]SUNCAT Center for Interface Science and Catalysis, Department of Chemical Engineering, Stanford University, 443 Via Ortega, Stanford, California 94305, United States

Supporting Information

ABSTRACT: The two-electron water oxidation reaction (2e-WOR) is a promising route for distributed electrochemical synthesis of hydrogen peroxide (H_2O_2), an effective and green oxidizer, bleaching agent, and antiseptic. To date, the best electrocatalyst for 2e-WOR, in terms of selectivity against the competing 4e-WOR to form O_2, is $BiVO_4$. Nevertheless, $BiVO_4$ is unstable and has a high overpotential of ∼340 mV at 0.2 mA/cm^2 for 2e-WOR. Herein, we use density functional theory to identify a new, efficient, selective, and stable electrocatalyst for 2e-WOR, i.e., the ternary oxide calcium stannate ($CaSnO_3$). Our experiments show that $CaSnO_3$ achieves an overpotential of 230 mV at 0.2 mA/cm^2, peak Faraday efficiency of 76% for 2e-WOR at 3.2 V vs the reversible hydrogen electrode (RHE), and stable performance for over 12 h, outperforming $BiVO_4$ in all aspects. This work demonstrates the promise of $CaSnO_3$ as a selective and cost-effective electrocatalyst candidate for H_2O_2 production from water oxidation.

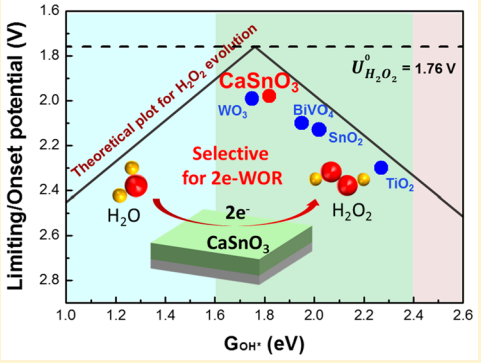

Hydrogen peroxide (H_2O_2) is among the 100 topmost important chemicals in the world and has broad industrial applications ranging from paper bleaching and chemical synthesis to environmental cleaning. Industrial production of H_2O_2 is achieved through the anthraquinone process, which requires large plants and infrastructures. Currently, there are only 60 H_2O_2 manufacturing plants in the world, which means the produced H_2O_2 must be transported to the point of use. However, H_2O_2 is unstable and potentially explosive at high concentrations, imposing safety challenges for transportation and storage. Alternatively, electrochemical processes provide the possibility for distributed on-site production of H_2O_2.[1−3] Recently, there has been a growing interest to use an electrochemical two-electron water oxidation (2e-WOR) process to produce H_2O_2 on-site.[4−8] The 2e-WOR process uses only water as the reactant and is much simpler than the commonly studied two-electron oxygen reduction reaction (ORR),[9] which must dissolve O_2 in water and/or gas-diffusion electrodes.

The adoption of 2e-WOR is hampered by the lack of an efficient, selective, and stable electrocatalyst. The catalytic performance of many metal oxides, such as WO_3, $BiVO_4$, SnO_2, TiO_2, CoO, La_2O_3, Al_2O_3, and ZrO_2,[10−12] has been tested for 2e-WOR. Among all of the oxides tested, $BiVO_4$ was identified as the premium candidate for 2e-WOR,[10,11,13] which achieves a Faraday efficiency (FE) of 30−70% and H_2O_2 generation rate of 0.7−5.6 μmol·min^{-1}·cm^{-2} over the bias range of 2.5−3.7 V vs RHE in the dark.[14] $BiVO_4$ also has the advantage of acting as both a photoanode and an electrocatalyst, producing photovoltage to reduce the applied potential needed.[14] However, $BiVO_4$ is unstable and toxic, imposing a challenge for practical implementation for H_2O_2 production.[15] Therefore, it is essential to identify a stable and nontoxic electrocatalyst for 2e-WOR that has comparable or even better catalytic properties than $BiVO_4$.

Inspired by the ternary nature of $BiVO_4$ and constrained by nontoxic elements, herein we employ density functional theory (DFT) to identify an efficient, selective, and stable electrocatalyst for 2e-WOR, resulting in the selection of the ternary oxide calcium stannate ($CaSnO_3$), which experimentally outperforms $BiVO_4$ and its binary component SnO_2 in all aspects. We show that $CaSnO_3$ achieves an overpotential of 230 mV at 0.2 mA/cm^2, a peak FE of 76% at 3.2 V vs RHE, and stable performance for over 12 h.

Received: November 27, 2018
Accepted: December 28, 2018
Published: December 28, 2018

DOI: 10.1021/acsenergylett.8b02303
ACS Energy Lett. 2019, 4, 352−357

We previously reported[3] that the catalytic activity toward the 2e-WOR (reaction R1) for evolving H_2O_2 is governed by the thermodynamics of reaction (reaction R1) at the surface of catalysts, which competes with 4e-WOR (reaction R2), and the one-electron water oxidation to form the OH radical (reaction R3).[16]

$$2H_2O \rightleftharpoons H_2O_2 + 2(H^+ + e^-) \qquad E^\circ = 1.76\ V \qquad (R1)$$

$$2H_2O \rightleftharpoons O_2 + 4(H^+ + e^-) \qquad E^\circ = 1.23\ V \qquad (R2)$$

$$H_2O \rightarrow OH^\bullet + (H^+ + e^-) \qquad E^\circ = 2.38\ V \qquad (R3)$$

The activity and selectivity of WORs are correlated with the adsorption free energies of several oxygenated reaction intermediates at the catalyst surface, including OH* (ΔG_{OH*}), O* (ΔG_{O*}), and OOH* (ΔG_{OOH*}).[3] Our previous study showed that catalysts with $\Delta G_{OH*} \approx 1.6-2.4$ eV and $\Delta G_{O*} > \sim 3.5$ are selective for H_2O_2 evolution (reaction R1), and either a stronger or weaker OH* bonding energy results in O_2 (reaction R2) and OH radical (reaction R3) evolutions, respectively.[3,14] Catalyst materials with $\Delta G_{OH*} \approx 1.76$ eV correspond to the best condition for H_2O_2 synthesis with zero theoretical overpotential.

Guided by the above theoretical framework, we used DFT to examine the catalytic activity and selectivity of $CaSnO_3$ and its binary component, SnO_2, for the 2e-WOR to evolve H_2O_2. To account for different types of active sites in both materials, we examined several low-index facets, including (001), (010), and (100) for $CaSnO_3$ and (100), (001), (110), and (111) for SnO_2. For the (010) and (100) facets of $CaSnO_3$, because the facet can be terminated through different patterns of oxygen coverage, we calculated the oxygen binding free energy (ΔG_{O*}) under different biases for different amounts of oxygen coverage.[17] Then, we identified the surface oxygen coverage in which oxygen binding becomes unfavorable ($\Delta G_{O*} > 0$) even at higher bias (2.0 V vs RHE). For example, Figure S1 in the Supporting Information illustrates that we gradually increased the oxygen coverage of $CaSnO_3$(100) to identify the most stable surface. For the saturated surfaces (e.g., Figure S1D–F), the oxygen binding becomes unfavorable ($\Delta G_{O*} > 0$) even at a high electrode potential, $-eU_{elec}$, where e and U_{elec} are the elementary charge and the electrode potential, respectively. We evaluated the catalytic activity of the facets when the surface is saturated with oxygen as the unsaturated surfaces are unstable under high oxidation potentials of 2e-WOR.

For the (001) facet of $CaSnO_3$, the catalytic activity for 2e-WOR was evaluated for two different termination patterns, exposed top Sn and bridge Ca–Ca sites, for the adsorption of the reaction intermediates (Figure 1). For the (010) and (100) facets of $CaSnO_3$, the active site is the Ca–Sn bridge (Figure 1). For SnO_2, the active sites are the top exposed Sn atoms (Figure 1). We also examined the contribution of surface lattice oxygens in the 2e-WOR, leaving the facets with oxygen defects. Our DFT results show that the surface-lattice oxygen forms strong bonds with the facets under the electrochemical reaction conditions, implying that the lattice oxygen is unlikely to participate in the WOR (Figure S2 in the Supporting Information).

For all of the above active sites, we calculated the adsorption free energy of the intermediates (ΔG_{OH*}, ΔG_{O*}, and ΔG_{OOH*}) to construct free energy diagrams of the reaction. Next, ΔG of the intermediates was shifted by $-eU_{elec}$ to account for the electrode potential and estimate the 2e-WOR limiting

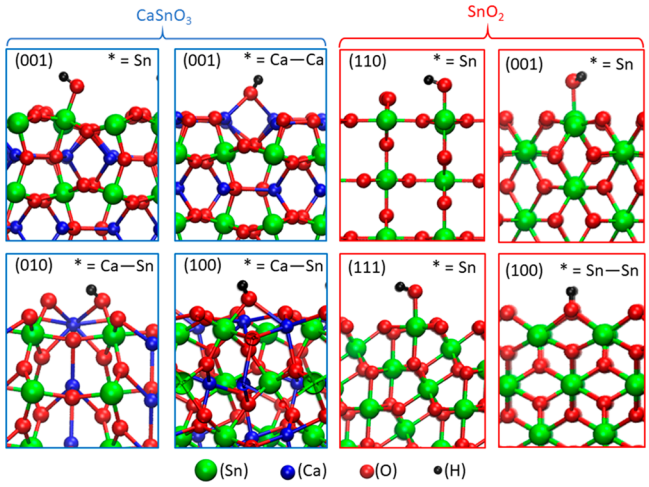

Figure 1. Side view of OH adsorption sites over the (001), (010), and (100) facets of $CaSnO_3$ and (110), (001), (100), and (111) facets of SnO_2. * denotes the active site for the intermediate reaction.

potential,[3] defined as the lowest potential at which all reaction steps are downhill in free energy. The calculated ΔG_{OH*} and U_L values are used to construct the activity volcano plots for both 2e- and 4e-WORs (Figure 2, solid black and dashed blue

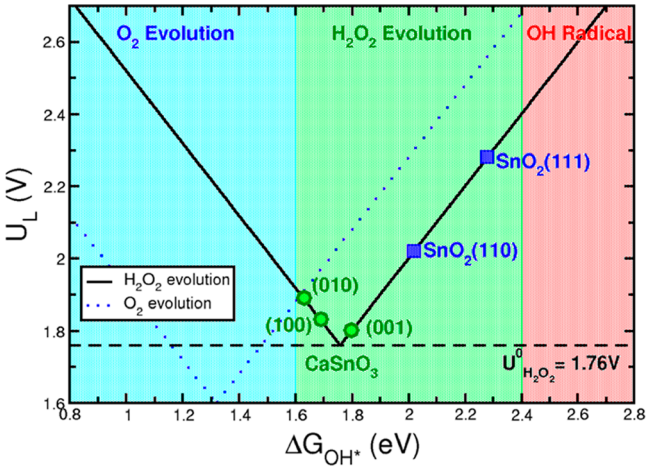

Figure 2. Theoretical activity volcano plots based on the calculated limiting potentials as a function of adsorption free energies of OH* (ΔG_{OH*}) for the 2e-WOR to evolve H_2O_2 (black solid line) and 4e-WOR to evolve O_2 (blue dotted line). Blue, green, and red highlighted areas correspond to the selective regions with O_2, H_2O_2, and OH radicals as dominant products, respectively. Of note, the free energy of solvated OH radical is ~2.4 eV (relative to water),[3] and thus, catalysts with $\Delta G_{OH*} > 2.4$ eV thermodynamically favor desorption of OH* and hence the formation of $^\bullet$OH(aq). Different facets of $CaSnO_3$ and SnO_2 are shown with green circles and blue squares, respectively.

lines, respectively).[3,14] The calculated U_L values can also be used to predict the reactions' overpotential, defined as $|U_L - U_{eq}|$, where U_{eq} is the equilibrium potential for the WORs. The three vertical zones from left to right in Figure 2 correspond to the selectivity regions toward O_2 evolution (reaction R2), H_2O_2 evolution (reaction R1), and OH radical formation (reaction R3). Clearly, the various $CaSnO_3$ and SnO_2 facets considered here favor the 2e-WOR over the other two WOR

DOI: 10.1021/acsenergylett.8b02303
ACS Energy Lett. 2019, 4, 352–357

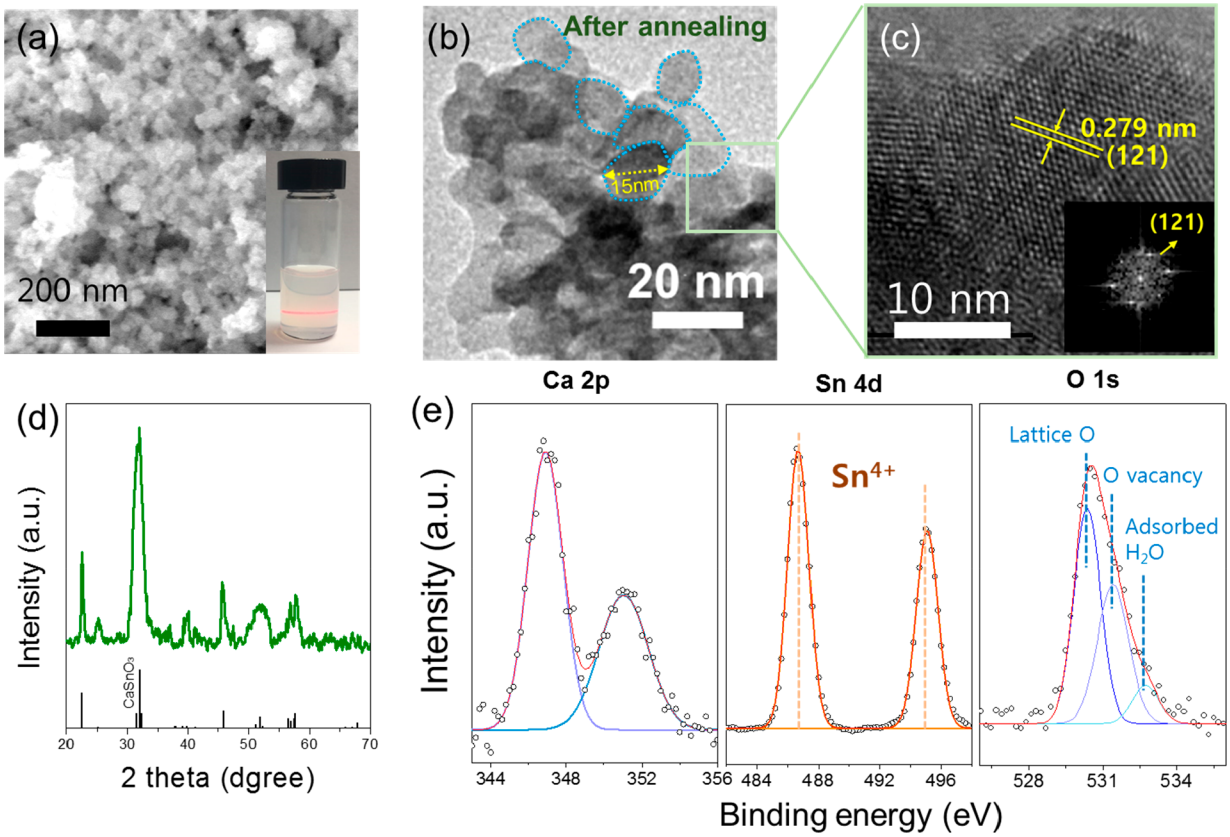

Figure 3. Characterization of synthesized $CaSnO_3$ nanoparticles. (a) SEM image of as-synthesized $CaSnO_3$ powder and photograph of dispersed $CaSnO_3$ colloidal solution (inset). (b) TEM and (c) HRTEM images of annealed $CaSnO_3$ nanoparticles (inset: reduced FFT image). (d) XRD pattern and (e) XPS spectra of annealed $CaSnO_3$ nanoparticles.

pathways. All three facets of $CaSnO_3$ show lower U_L values than the two facets of SnO_2. The $CaSnO_3$(100) and (010) facets lie on the left side of the theoretical activity of the 2e-WOR volcano plot, where we expect that both 2e- and 4e-WOR occur in parallel, as observed in the previously studied oxides such as WO_3.[14] Among all of the facets, the $CaSnO_3$(001) facet appears to have the highest activity and selectivity. The U_L values of the $CaSnO_3$(001) facet are 1.81 eV for the surface Sn^{4+} and 1.80 eV for Ca−Ca bridge sites, corresponding to a ∼40−50 mV overpotential for H_2O_2 synthesis. These overpotentials are about 150−200 mV lower than the previously reported values on the other oxides such as $BiVO_4$.[14]

To verify our theoretical calculation results, we synthesized $CaSnO_3$ nanoparticles (Figure 3a) via the reaction of $SnCl_2$ and $CaCl_2$ in H_2O_2 through the colloidal synthesis method (see the Experimental Methods section for details).[12] As shown in the inset of Figure 3a, when a laser beam (600 nm) passed through the $CaSnO_3$ dispersed solution, we observed a clear visible beam path, indicating that the $CaSnO_3$ nanoparticles were well dispersed in the solvent based on the Tyndall effect. The as-synthesized $CaSnO_3$ nanoparticles were amorphous (Figure S3a,b) and were crystallized after coating on F:SnO_2 (FTO) substrates followed by annealing at 600 °C for 2 h. The annealed nanoparticles have an average diameter of ∼15 nm (Figure 3b) and are crystalline, as evidenced by transmission electron microscopy (TEM), reduced fast Fourier transform (FFT) images, and X-ray diffraction (XRD) (Figure 3c,d). The high-resolution TEM image (Figure 3c) shows a lattice spacing of 0.279 nm, an indication of the (121) crystal planes of $CaSnO_3$. The chemical composition of $CaSnO_3$ was confirmed using X-ray photoelectron spectroscopy (XPS). The XPS spectra in Figure 3e show dominant Ca 2p peaks at 346.9 and 350.5 eV, Sn 4d peaks at 485.4 and 493.9 eV, and O 1s peaks at 530.3, 531.4, and 532.7 eV, confirming the oxidation states of Ca^{2+} and Sn^{4+}. The peaks at 530.3 and 531.4 eV are attributed to the O^{2-} ions and the oxygen vacancies in the crystal structure of the perovskite oxide structure (ABO_3), respectively.[18−20] The 532.7 eV peak corresponds to the surface adsorption oxygen.[18−20] For reference, the as-synthesized $CaSnO_3$ without 600 °C annealing contains Sn^{2+} and more oxygen vacancies (Figure S4). Those characterization results show that the 600 °C annealing step is necessary to achieve the desired crystallinity and chemical states of $CaSnO_3$ for the following electrochemical studies.

To characterize the electrochemical properties, we coated the $CaSnO_3$ nanoparticles onto conductive FTO substrates. This was achieved by first dispersing as-synthesized $CaSnO_3$ nanoparticles in a mixture of chloroform and methanol (inset image, Figure 3a), then spin-coating the colloidal solution onto FTO substrates, and finally annealing at 600 °C for 2 h. Because $CaSnO_3$ (bandgap ≈ 4.4 eV) is not conductive,[21−23] the coated film thickness is optimized to be ∼80 nm to compromise between conductivity and good coverage over FTO (Figures S5−S8). The comparison sample of SnO_2 films was prepared by the sol−gel method and annealed step by step at 180 °C for 30 min and at 450 °C for 1 h. (Figure S9; see the Experimental Methods section for details). The XRD pattern of the annealed SnO_2 film (Figure S10) matches well with the pure crystalline SnO_2 (JCPDS card # 71-0652). The

DOI: 10.1021/acsenergylett.8b02303
ACS Energy Lett. 2019, 4, 352−357

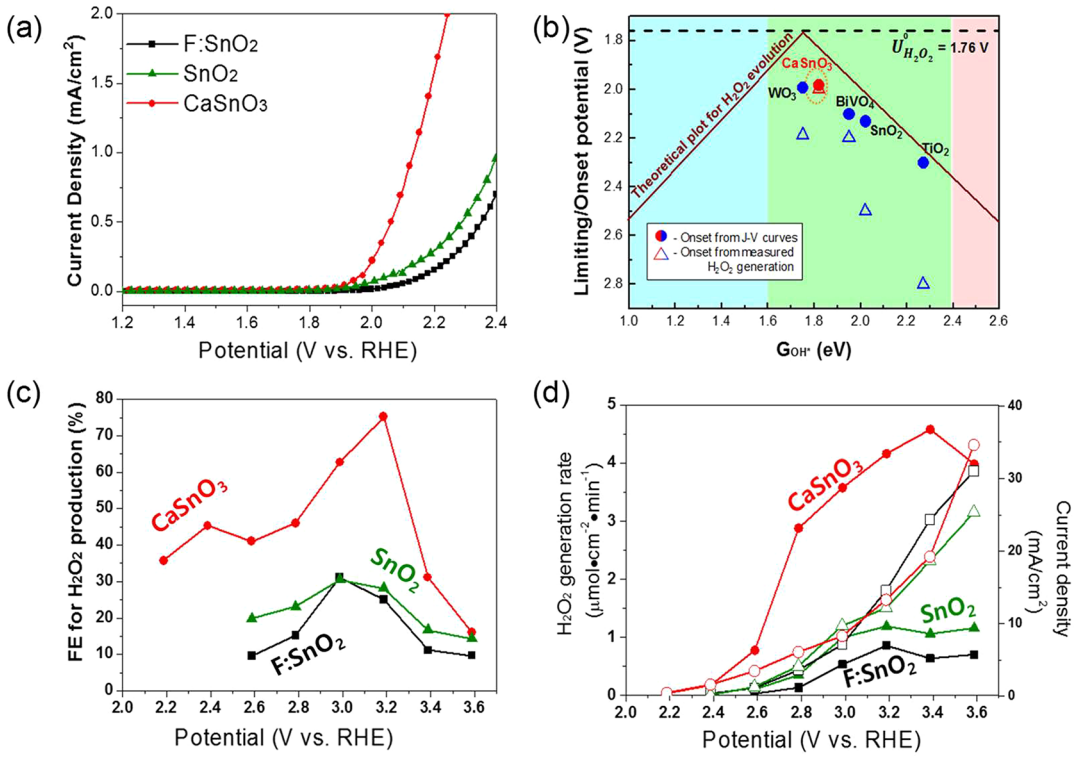

Figure 4. Electrochemical performance of $CaSnO_3$ in comparison with FTO ($F:SnO_2$) and SnO_2. (a) Current vs potential (J–V) curves. (b) Theoretical activity volcano plots based on the calculated limiting potentials as a function of adsorption free energies of OH* (ΔG_{OH^*}). Previously studied metal oxides[14] are shown for comparison. Circles are the experimental onset potential at which the current density reaches 0.2 mA/cm^2. Triangles are the experimental onset potential at which the H_2O_2 concentration reaches 1 ppm after 10 min of testing with 20 mL of 2 M $KHCO_3$ electrolyte. (c) FE and (d) generation rate of H_2O_2 (left y axis, solid symbols, circle, $CaSnO_3$; triangle, SnO_2; square, $F:SnO_2$) and the current density (right y-axis, hollow symbols) as a function of potential.

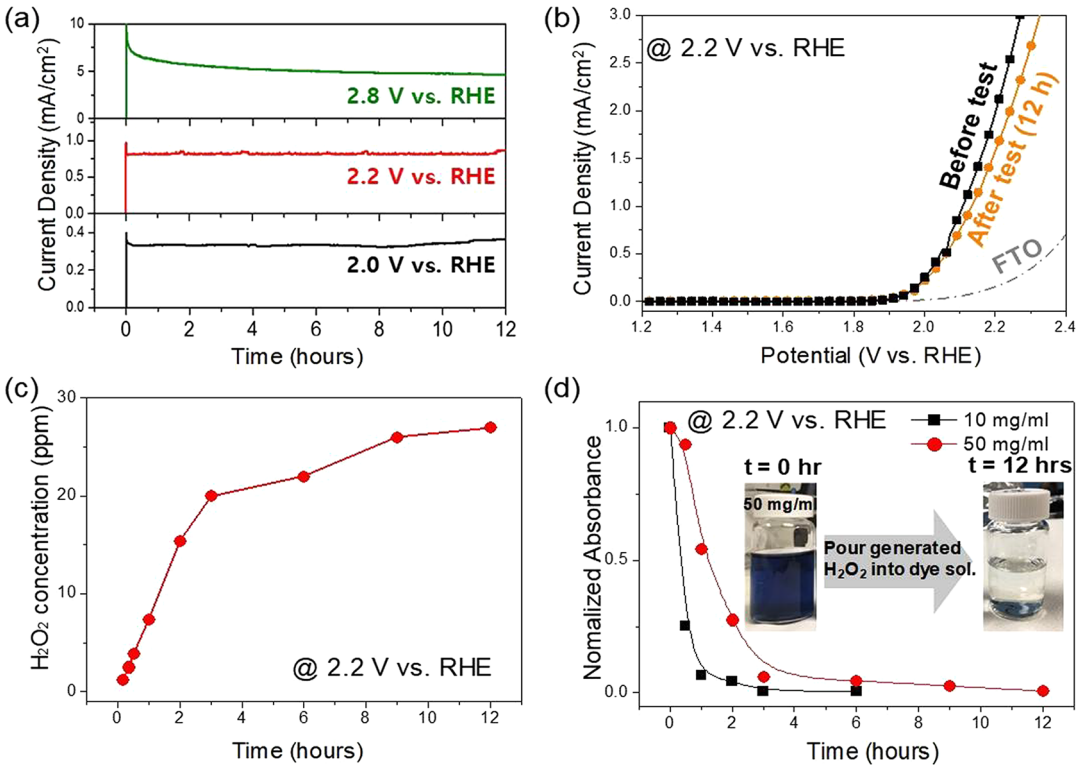

Figure 5. (a) Stability tests of J–t curves of $CaSnO_3$ under different applied biases. (b) J–V curve of $CaSnO_3$ under 2.2 V vs RHE before and after 12 h of J–t measurement shown in (a). (c) H_2O_2 concentration vs time. (d) Dye decolorization test at 2.2 V vs RHE with two dye concentrations and periodic addition of electrolyte with generated H_2O_2.

DOI: 10.1021/acsenergylett.8b02303
ACS Energy Lett. 2019, 4, 352–357

electrochemical active surface area of SnO_2 estimated using the cyclic voltammetry (CV) measurements is similar to that of $CaSnO_3$ (Figure S11). This allows one to merely compare their intrinsic surface catalytic property differences.

The catalytic properties of $CaSnO_3$ nanoparticles for 2e-WOR were studied in 2 M $KHCO_3$ electrolyte (pH ≈ 8.3) using a standard three-electrode configuration, with $CaSnO_3$ on FTO as the working electrode, Ag/AgCl as the reference electrode, and carbon paper as the counter electrode. Figure 4a shows the current−potential ($J-V$) curves of $CaSnO_3$, SnO_2, and the bare FTO (F:SnO_2). $CaSnO_3$ has a much lower onset potential and higher current density than both SnO_2 and F:SnO_2. We defined the onset potential as the applied bias at which the current density reaches 0.2 mA/cm^2. The onset potentials for $CaSnO_3$ and SnO_2 are 1.99 and 2.13 V vs RHE, respectively. Figure 4b compares the onset potentials of $CaSnO_3$, SnO_2, and several other reported oxides[14] (circle symbols) together with the DFT results (Figure 2). Please note that the y axis of Figure 4b shows the onset potential in the reverse order of Figure 2; therefore, the tip of the volcano in Figure 4b corresponds to the highest catalytic activity. Because not all current will evolve H_2O_2 due to the competing reactions R2 and R3, we also plotted the onset potentials of those metal oxides (Figure 4b, triangles) based on a different definition, which is the potential for the H_2O_2 concentration reaching 1 ppm after 10 min of testing. Regardless of the definition of the onset potential, $CaSnO_3$ shows the lowest onset potential, which is equivalent to the highest catalytic activity, toward 2e-WOR among all of the oxides reported. We also tested the effect of the pH value of the electrolyte on the H_2O_2 production by adjusting the pH value of $KHCO_3$ electrolyte by adding H_2SO_4 or KOH, and the results show that a near-neutral pH value is the best condition for generating H_2O_2 (Figure S12).

The selectivity of $CaSnO_3$ for 2e-WOR is evaluated in terms of the FE for H_2O_2 (Figure 4c) and the H_2O_2 generation rate (Figure 4d) as a function of the applied potential. For both properties, $CaSnO_3$ shows values 2−5 times higher than those of SnO_2 and F:SnO_2 over the tested bias range of 2.2−3.6 V vs RHE. Notably, the peak FE of $CaSnO_3$ reaches 76% at 3.2 V vs RHE, which exceeds those of F:SnO_2, SnO_2 (∼32%), and all other reported metal oxides.[14] For reference, $BiVO_4$, reported as the best electrocatalyst for 2e-WOR so far, achieves a FE of 70% at 3.1 V vs RHE.

The stability of $CaSnO_3$ for 2e-WOR was tested by measuring the current density vs time under several biases (2.0, 2.2, and 2.8 V vs RHE) for 12 h. The results in Figure 5a show that $CaSnO_3$ is quite stable at 2.0 V vs RHE and becomes less stable with increasing bias. Figure 5b shows the $J-V$ curves before and after the 12 h amperometric test at 2.2 V vs RHE, which shows a small current change. We also monitored the accumulation of H_2O_2 in the electrolyte solution (volume: 30 mL) under 2.2 V vs RHE for 12 h. Figure 5c shows that the H_2O_2 concentration initially shows a faster linear increase and then slows down with time. A similar trend was also observed for other metal oxides for 2e-WOR.[14,24] Factors contributing to this H_2O_2 concentration saturation phenomenom include the tendency of H_2O_2 to be further oxidized by holes ($H_2O_2 \rightleftharpoons O_2 + 2H^+ + 2e^-$) and to decompose ($2H_2O_2 \rightleftharpoons O_2 + 2H_2O$), and the inhibitive effect on reaction R1 from the higher concentration of H_2O_2 due to Le Chatlier's principle for chemical equilibrium. The production of H_2O_2 was further confirmed by the decolorization of the dye solution (reactive black 5). The dye solution was prepared in two different concentrations, 10 and 50 mg/mL, and 15 mL of electrolyte containing the generated H_2O_2 was periodically withdrawn and added to the dyes. The decay of the dye color was quantified using UV−vis absorbance measurement as a function of time. Figure 5d shows that both concentrations of the dye solution effectively degraded as more H_2O_2 was added. The inset in Figure 5d shows that the dye solution (50 mg/mL) changes from blue to clear after 12 h.

To test the performance under the condition of the highest FE, we also measured the stability of $CaSnO_3$ for 2e-WOR under 3.2 V vs RHE for 12 h in terms of the current density and the generated amount of H_2O_2 and O_2 as a function of time (as Figure S13). The stability test shows that $CaSnO_3$ has fair stability under 3.2 V for the 12 h measurement. In the beginning, $CaSnO_3$ evolves more H_2O_2. As the concentration of H_2O_2 increases, the production of O_2 is increased for two reasons. One is that a higher concentration of H_2O_2 inhibits the 2-electron water oxidation due to the Le Chatelier's principle as it will shift the equilibrium to the side that would reduce the concentration of H_2O_2. The other is that H_2O_2 is not stable at a high applied bias as well.

In summary, we have demonstrated that $CaSnO_3$ is an efficient, selective, and relatively stable electrocatalyst for 2e-WOR for H_2O_2 production. Our DFT calculation results show that several low-index facets of $CaSnO_3$, including (001), (010), and (100), exhibit a lower limiting potential than the (110) and (111) facets of SnO_2. The $CaSnO_3$(001) facet shows the best activity and selectivity for 2e-WOR. Experimentally, we synthesized crystalline $CaSnO_3$ nanoparticles (∼15 nm in diameter), which exhibit the lowest overpotential of 230 mV at 0.2 mA/cm^2 among all of the metal oxides reported. $CaSnO_3$ nanoparticles show good selectivity toward 2e-WOR, with a peak FE of 76% at 3.2 V vs RHE and stable performance for over 12 h at 2.2 V vs RHE. Given the excellent catalytic performance and low cost, $CaSnO_3$ is a great electrocatalyst candidate for H_2O_2 production through water oxidation. Nevertheless, $CaSnO_3$ is hazardous to the aquatic environment,[25] and therefore, the search for a nontoxic and good catalyst for water oxidation is crucial for this field for future works.

■ ASSOCIATED CONTENT

Supporting Information

The Supporting Information is available free of charge on the ACS Publications website at DOI: 10.1021/acsenergylett.8b02303.

Experimental methods and supporting data (PDF)

■ AUTHOR INFORMATION

Corresponding Authors

*E-mail: hsjung1@skku.edu (H.S.J.).
*E-mail: samiras@stanford.edu (S.S.).
*E-mail: xlzheng@stanford.edu (X.Z.).

ORCID

So Yeon Park: 0000-0001-6774-0941
Xinjian Shi: 0000-0002-1998-6936
Hyun Suk Jung: 0000-0002-7803-6930
Samira Siahrostami: 0000-0002-1192-4634
Xiaolin Zheng: 0000-0002-8889-7873

DOI: 10.1021/acsenergylett.8b02303
ACS Energy Lett. 2019, 4, 352−357

Author Contributions

[#]S.Y.P., H.A., and X.S. contributed equally to this work.

Notes

The authors declare no competing financial interest.

■ ACKNOWLEDGMENTS

X.Z. would like to thank the Stanford Woods Institute for the Environment and the Stanford Natural Gas Initiative for their generous support. This research was supported by the Basic Research Lab Program through the National Research Foundation of Korea (NRF) funded by the Ministry of Science, ICT & Future Planning (2017R1A2B3010927, 2018M3C1B7021994, and 2016M3D1A1027664).

■ REFERENCES

(1) Chen, Z. H.; Chen, S. C.; Siahrostami, S.; Chakthranont, P.; Hahn, C.; Nordlund, D.; Dimosthenis, S.; Norskov, J.; Bao, Z. N.; Jaramillo, T. Development of a reactor with carbon catalysts for modular-scale, low-cost electrochemical generation of H_2O_2. *React. Chem. Eng.* **2017**, *2*, 239−245.

(2) Siahrostami, S.; Verdaguer-Casadevall, A.; Karamad, M.; Deiana, D.; Malacrida, P.; Wickman, B.; Escudero-Escribano, M.; Paoli, E. A.; Frydendal, R.; Hansen, T. W.; Chorkendorff, I.; et al. Enabling direct H_2O_2 production through rational electrocatalyst design. *Nat. Mater.* **2013**, *12*, 1137−1143.

(3) Siahrostami, S.; Li, G. L.; Viswanathan, V.; Norskov, J. K. One- or Two-Electron Water Oxidation, Hydroxyl Radical, or H_2O_2 Evolution. *J. Phys. Chem. Lett.* **2017**, *8*, 1157−1160.

(4) Campos, M.; Siriwatcharapiboon, W.; Potter, R. J.; Horswell, S. L. Selectivity of Cobalt-Based Catalysts Towards Hydrogen Peroxide Formation during the Reduction of Oxygen. *Catal. Today* **2013**, *202*, 135−143.

(5) Jirkovský, J. S.; Panas, I.; Ahlberg, E.; Halasa, M.; Romani, S.; Schiffrin, D. J. Single Atom Hot-Spots at Au−Pd Nanoalloys for Electrocatalytic H_2O_2 Production. *J. Am. Chem. Soc.* **2011**, *133*, 19432−19441.

(6) Siahrostami, S.; Björketun, M. E.; Strasser, P.; Greeley, J.; Rossmeisl, J. Tandem Cathode for Proton Exchange Membrane Fuel Cells. *Phys. Chem. Chem. Phys.* **2013**, *15*, 9326−9334.

(7) Siahrostami, S.; Verdaguer-Casadevall, A.; Karamad, M.; Deiana, D.; Malacrida, P.; Wickman, B.; Escudero-Escribano, M.; Paoli, E. A.; Frydendal, R.; Hansen, T. W.; et al. Enabling Direct H_2O_2 Production through Rational Electrocatalyst Design. *Nat. Mater.* **2013**, *12*, 1137.

(8) Verdaguer-Casadevall, A.; Deiana, D.; Karamad, M.; Siahrostami, S.; Malacrida, P.; Hansen, T. W.; Rossmeisl, J.; Chorkendorff, I.; Stephens, I. E. Trends in the Electrochemical Synthesis of H_2O_2: Enhancing Activity and Selectivity by Electrocatalytic Site Engineering. *Nano Lett.* **2014**, *14*, 1603−1608.

(9) Chai, G. L.; Hou, Z. F.; Ikeda, T.; Terakura, K. Two-Electron Oxygen Reduction on Carbon Materials Catalysts: Mechanisms and Active Sites. *J. Phys. Chem. C* **2017**, *121*, 14524−14533.

(10) Fuku, K.; Miyase, Y.; Miseki, Y.; Gunji, T.; Sayama, K. Enhanced Oxidative Hydrogen Peroxide Production on Conducting Glass Anodes Modified with Metal Oxides. *ChemistrySelect* **2016**, *1*, 5721−5726.

(11) Fuku, K.; Sayama, K. Efficient Oxidative Hydrogen Peroxide Production and Accumulation in Photoelectrochemical Water Splitting using a Tungsten Trioxide/bismuth Vanadate Photoanode. *Chem. Commun.* **2016**, *52*, 5406−5409.

(12) Shin, S. S.; Yeom, E. J.; Yang, W. S.; Hur, S.; Kim, M. G.; Im, J.; Seo, J.; Noh, J. H.; Seok, S. I. Colloidally Prepared La-doped $BaSnO_3$ Electrodes for Efficient, Photostable Perovskite Solar Cells. *Science* **2017**, *356*, 167−171.

(13) Fuku, K.; Miyase, Y.; Miseki, Y.; Gunji, T.; Sayama, K. WO_3/$BiVO_4$ Photoanode Coated with Mesoporous Al_2O_3 Layer for Oxidative Production of Hydrogen Peroxide from Water with High Selectivity. *RSC Adv.* **2017**, *7*, 47619−47623.

(14) Shi, X.; Siahrostami, S.; Li, G. L.; Zhang, Y.; Chakthranont, P.; Studt, F.; Jaramillo, T. F.; Zheng, X.; Norskov, J. K. Understanding Activity Trends in Electrochemical Water Oxidation to Form Hydrogen Peroxide. *Nat. Commun.* **2017**, *8*, 701.

(15) Kruithof, J. C.; Kamp, P. C.; Martijn, B. J. UV/H_2O_2 Treatment: a Practical Solution for Organic Contaminant Control and Primary Disinfection. *Ozone: Sci. Eng.* **2007**, *29*, 273−280.

(16) Bard, A. J.; Parsons, R.; Jordan, J. *Standard potentials in aqueous solution*, 1st ed.; M. Dekker: New York, 1985.

(17) Hansen, H. A.; Rossmeisl, J.; Norskov, J. K. Surface Pourbaix Diagrams and Oxygen Reduction Activity of Pt, Ag and Ni(111) Surfaces Studied by DFT. *Phys. Chem. Chem. Phys.* **2008**, *10*, 3722−3730.

(18) Zhang, N.; Chen, D.; Niu, F.; Wang, S.; Qin, L.; Huang, Y. Enhanced Visible Light Photocatalytic Activity of Gd-Doped $BiFeO_3$ Nanoparticles and Mechanism Insight. *Sci. Rep.* **2016**, *6*, 26467.

(19) Teraoka, Y.; Yoshimatsu, M.; Yamazoe, N.; Seiyama, T. Oxygen-Sorptive Properties and Defect Structure of Perovskite-Type Oxides. *Chem. Lett.* **1984**, *13*, 893−896.

(20) Chen, D.; Niu, F.; Qin, L. S.; Wang, S.; Zhang, N.; Huang, Y. X. Defective $BiFeO_3$ with Surface Oxygen Vacancies: Facile Synthesis and Mechanism Insight into Photocatalytic Performance. *Sol. Energy Mater. Sol. Cells* **2017**, *171*, 24−32.

(21) Mizoguchi, H.; Eng, H. W.; Woodward, P. M. Probing the Electronic Structures of Ternary Perovskite and Pyrochlore Oxides Containing Sn^{4+} or Sb^{5+}. *Inorg. Chem.* **2004**, *43*, 1667−1680.

(22) Fierro, J. L. G. *Metal oxides: chemistry and applications*; CRC Press: Madrid, Spain, 2005.

(23) Yoshida, M.; Katsumata, T.; Inaguma, Y. High-Pressure Synthesis, Crystal and Electronic Structures, and Transport Properties of a Novel Perovskite $HgSnO_3$. *Inorg. Chem.* **2008**, *47*, 6296−6302.

(24) Shi, X. J.; Zhang, Y. R.; Siahrostami, S.; Zheng, X. L. Light-Driven $BiVO_4$-C Fuel Cell with Simultaneous Production of H_2O_2. *Adv. Energy Mater.* **2018**, *8*, 1801158.

(25) Materion. *Safety data sheet - calcium stannate*, version 01; 2018; pp 1−7.

DOI: 10.1021/acsenergylett.8b02303
ACS Energy Lett. 2019, 4, 352−357